Time–Temperature–Solvent Modulated Zn–Fe Bimetallic MOFs: Correlating Structural Dynamics with Optical, Redox, and Dopamine Sensing Performance

Deepika Sharma[a], Pallavi Kadian[a], Rajat Sharma[b], Jaspreet Kaur Randhawa[b*]

a School of Chemical Sciences, Indian Institute of Technology, Mandi (175005), India

b School of Mechanical and Materials Engineering Indian Institute of Technology, Mandi (175005), India

Corresponding Author: jaspreet@iitmandi.ac.in

(**Supplementary Information**)

Table of contents

detected elements, and (b(i)) highlights the deconvoluted Fe 2p spectrum of the pure Fe MOF for comparison. The subsequent subpanels (ii)–(viii) in both (a) and (b) correspond to the individual samples studied: (ii) ZnFe MOF, (iii) ZnFe 12, (iv) ZnFe 24, (v) ZnFe 1:1, (vi) ZnFe 2:1, (vii) ZnFe 100, and (viii) ZnFe 140. These spectra allow a clear comparison of the Zn and Fe chemical states across the different compositions and synthesis conditions.

3.6. Figure S6: Elemental composition analysis of MOFs using TEM-EDAX, with elemental identities indicated at the top of each spectrum: (a) Fe-MOF, (b) ZnFe-12, (c) ZnFe-MOF, (d) ZnFe-24, (e) ZnFe-1:1, (f) ZnFe-100, (g) ZnFe-2:1, and (h) ZnFe-140.

3.7. Figure S7: BET surface area analysis of (a) ZnFe-MOF, (b) ZnFe-24, (c) ZnFe-2:1, (d) ZnFe-140, (e) Fe-MOF, (f) ZnFe-12, (g) ZnFe-1:1, and (h) ZnFe-100, illustrating the textural properties and porosity variations among the synthesized MOFs.

3.8. Figure S8: BJH pore size distribution of (a) ZnFe-MOF, (b) ZnFe-24, (c) ZnFe-2:1, (d) ZnFe-140, (e) Fe-MOF, (f) ZnFe-12, (g) ZnFe-1:1, and (h) ZnFe-100, highlighting the mesoporous characteristics and structural variations of the synthesized MOFs.

3.9. Figure S9: Thermogravimetric analysis (TGA) of MOF samples: (a) Comparison between ZnFe-MOF and Fe-MOF; (b) Effect of reaction time; (c) Influence of solvent; (d) Impact of synthesis temperature on thermal stability.

3.10. Figure S10: Raman spectra of ZnFe-MOF samples synthesized under varying conditions: (a) Effect of reaction time, (b) Influence of solvent, (c) Impact of synthesis temperature on molecular structure.

3.11. Figure S11: Rietveld Refined patterns of (a) ZnFe 140 (b) ZnFe MOF, (c) ZnFe 2:1, Where (i)$CHCl_3$, (ii) DMF, (iii) MeOH and (iv) H_2O represents different solvents in which respective samples were soaked. The grey lines are simulated graph NH_2-MIL-88B , orange lines are obtained PXRD pattern of different MOFs , green lines are difference between simulated and obtained pattern , yellow lines are background line and blue drop lines are Bragg's positions.

3.12. Figure S12: Time-dependent fluorescence spectra of (a) ZnFe-MOF and (b) Fe-MOF, illustrating the evolution of fluorescence behaviour over time.

3.13. Figure S13: (a) Comparison of ZnFe MOF with Fe MOF under same conditions for Dopamine sensing (b) Bare GCE at varying applied potential and (c) ZnFe MOF modified GCE with varying applied potential.

4. List of Tables

4.1. Table S1: Summary of crystallite size, lattice constants, cell volume, space group and crystallographic Rietveld refinement parameters for the MOF samples.

4.2. Table S2: XPS atomic weight percentage of Zinc, Iron, Oxygen, Nitrogen and Carbon in all MOFs.

4.3. Table S3 Breathing behaviour: variation in pore width in various solvents for ZnFe 140, ZnFe MOF, and ZnFe 2:1.

4.4. Table S4: Breathing Behaviour -Variation via Rietveld refinement in various MOFs ZnFe 140, ZnFe MOF and ZnFe 2:1.

4.5. Table S5: Comparison table of recently reported Dopamine sensors with their linear range and limit of detection.

Material Characterization

Morphological analysis was performed utilizing the NOVA Nano SEM 450 Field Emission Scanning Electron Microscope (FESEM) at an accelerating voltage of 10 kV. The average size of SEM images was ascertained utilizing Image J program. Energy dispersive X-ray spectroscopy (EDAX) was employed to analyse the elemental distribution within the ZnFe MOF and Fe MOF. High-resolution imaging was conducted using an FEI Tecnai Transmission Electron Microscope (TEM) operating at 200 kV and featuring a LaB6 filament. X-ray Diffraction (XRD) analysis was conducted using a Rigaku Smart Lab X-ray diffractometer, utilizing Cu-Kα radiation (λ = 1.54 Å) at 45 kV and 100 mA, under ambient temperature conditions. The investigation covered a 2θ range of 5° to 40°, with a scanning rate of 2° min^{-1} and a step size of 0.02°. X-ray Photoelectron Spectroscopy (XPS) examination was performed with a VG ESCALAB250 electron spectrometer, employing monochromatic Al Kα (1486.6 eV) radiation at 15 kV and 10 mA. Binding energies were calibrated to the C1s peak (284.0 eV) before data analysis. The observed spectra were peak fitted using Avantage data processing software (Shirley-type background). UV-vis spectroscopy (Shimadzu UV-2450)

was used to determine optical properties. Fourier Transform Infrared Spectroscopy (FTIR) spectra from 400 to 4000 cm^{-1} were obtained using a PerkinElmer UATR-Two Spectrometer. The adsorption/desorption isotherms and pore volumes of the adsorbents were determined using nitrogen adsorption–desorption isotherms, measured at 77 K using a Quanta chrome Autosorb 1C Brunauer–Emmett–Teller system. Magnetic force microscopy (MFM) was conducted using a Dimension ICON MFM (Bruker) in tapping mode, with a scanning rate of 0.9 Hz with optimised lift height. Thermogravimetric Analysis (TGA) was conducted utilizing a Netzsch STA 449 F1 Jupiter apparatus (Netzsch, Germany). Samples weighing 2–3 mg were positioned in typical alumina pans with alumina lids and a central pinhole. A vacant crucible functioned as the standard. Heating initiated from Room temperature to 800°C at a rate of 10°C min^{-1} in a nitrogen environment with a flow rate of 60 mL min^{-1}. Fluorescence analysis was performed at 20 °C using a Varian TM Cary Eclipse fluorescence spectrometer (Agilent Technologies, USA). EPR spectra were obtained at 295K using a Bruker Bio Spin spectrometer operating at 2.5 GHz. Confocal imaging was done using Nikon Eclipse Ti inverted microscope and images were acquired using Nikon Nis-Element software.

Electrochemical sensing

ZnFe MOF was used as the working electrode, platinum wire as the counter electrode, and saturated calomel electrode (SCE) as the reference electrode in a standard three-electrode configuration for electrochemical sensing measurements using an electrochemical workstation (Metrohm Autolab, AUT86502). Measurements using cyclic voltammetry (CV) were carried out in the potential range of -1 to 1 V. To assess the electrochemical sensing capabilities of the ZnFe MOF samples toward DA, amperometric measurements were performed at an applied potential of 0.5 V vs. SCE in 0.1 M phosphate buffer saline (PBS) solution (pH 7). The electrode was prepared by dispersing 1 mg of the MOF sample in a 1 mL solution that contained 20 µL of Nafion and 980 µL of ethanol to create a 1 mg mL-1 dispersion. Because of its exceptional mechanical stability, high proton conductivity, and good chemical and thermal stabilities, Nafion has been used as a proton exchange membrane. The sample adheres well to the GCE when Nafion is used. Before being used for electrochemical measurements, 10 µL of the suspension was then applied to the GCE's surface and left to naturally dry at room temperature.

Synthesis Procedure

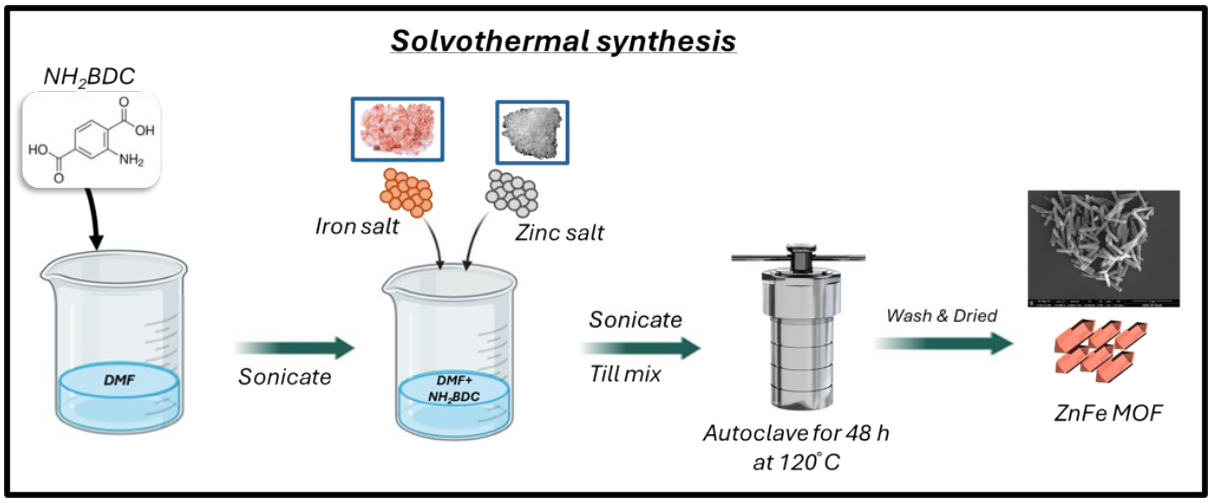

Figure S1: *Schematic illustration of ZnFe MOF synthesis.*

UV

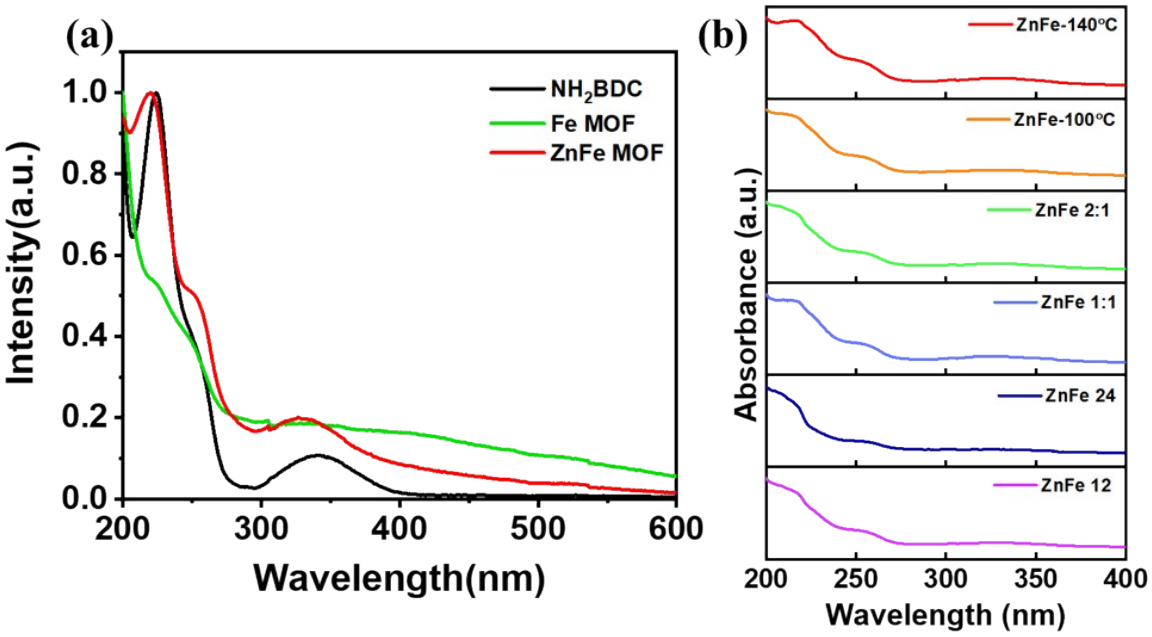

Figure S2: *(a) UV–Vis spectra of NH₂-BDC, Fe-MOF, and ZnFe-MOF, (b) UV–Vis spectra showing the influence of reaction parameters, including time, solvent, and temperature, on the synthesized MOFs.*

Tauc Plot

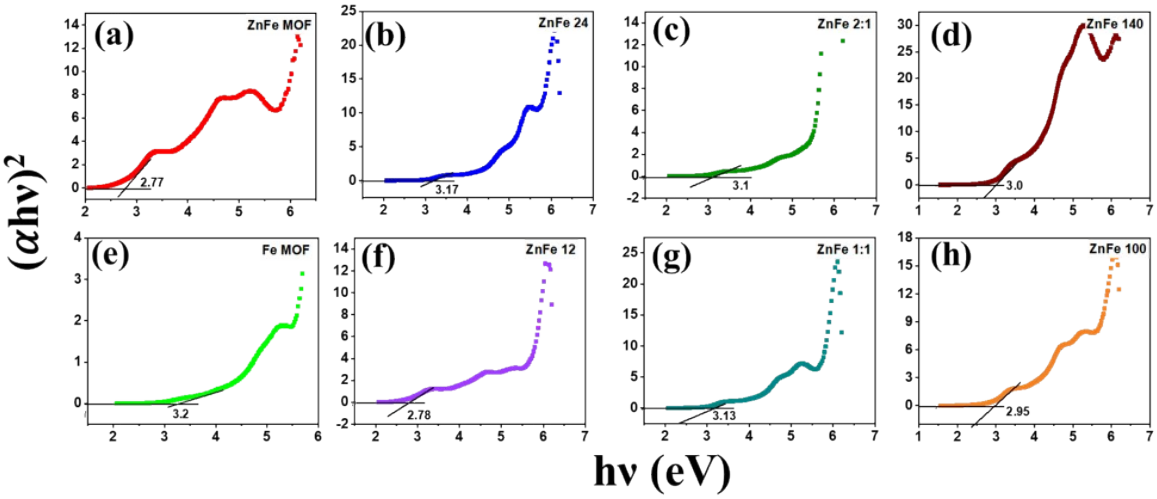

Figure S3*: Tauc plots of (a) ZnFe-MOF, (b) ZnFe-24, (c) ZnFe-2:1, (d) ZnFe-140, (e) Fe-MOF, (f) ZnFe-12, (g) ZnFe-1:1, and (h) ZnFe-100, illustrating the optical band gap variations across different compositions and synthesis conditions.*

FTIR

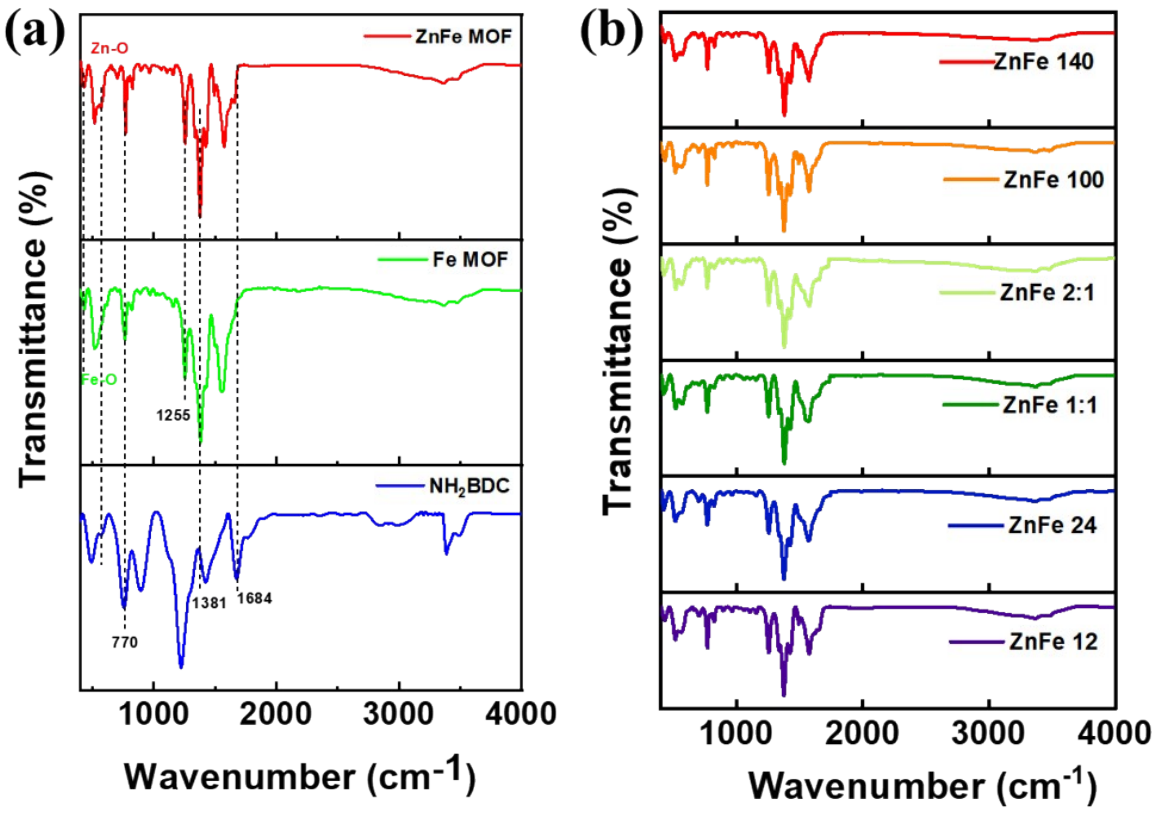

***Figure S4**:(a) FTIR spectra of NH_2-BDC, Fe-MOF, and ZnFe-MOF, (b) FTIR spectra of ZnFe-MOF samples synthesized under varying conditions of time, solvent, and temperature.*

XPS

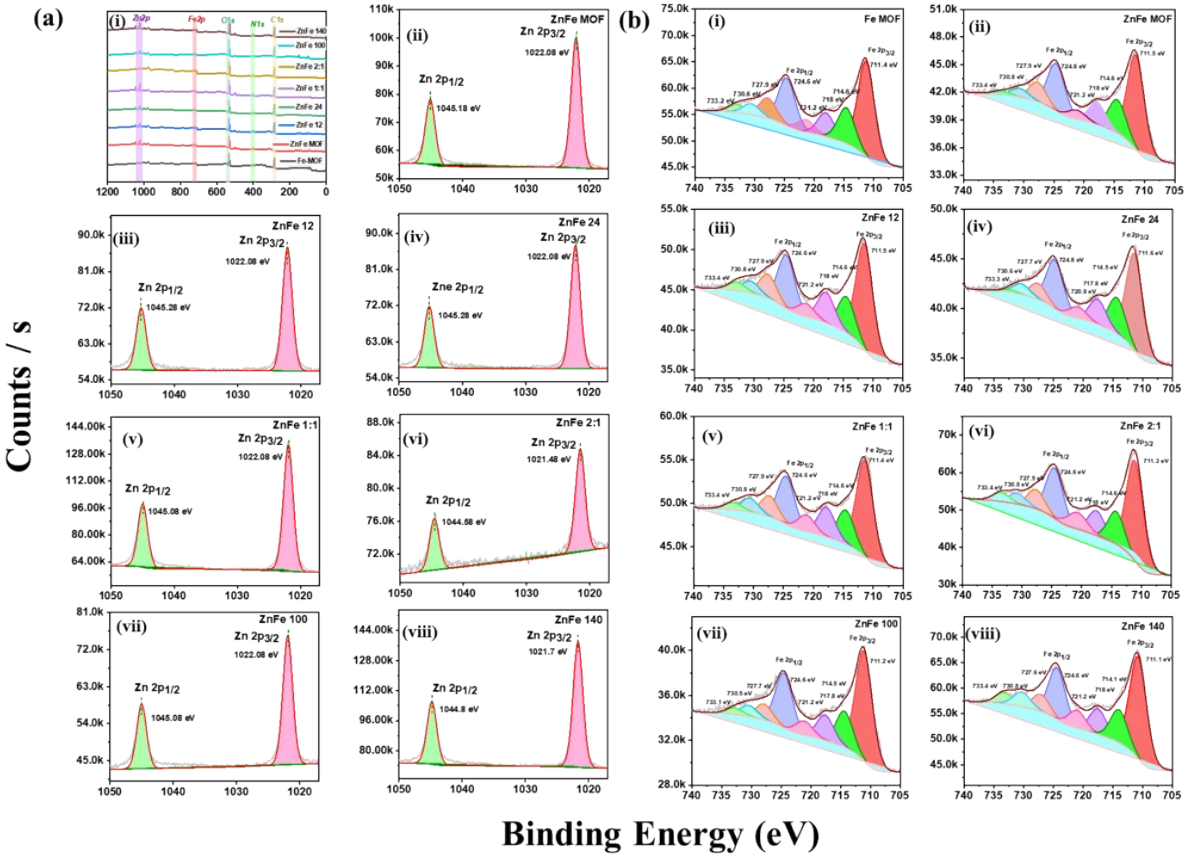

***Figure S5 : XPS spectra of different MOF samples.** Panel (a) shows the Zn 2p spectra after deconvolution, while panel (b) shows the deconvoluted Fe 2p spectra. In addition, (a(i)) presents the full survey spectrum of all MOFs, giving an overview of all the detected elements, and (b(i)) highlights the deconvoluted Fe 2p spectrum of the pure Fe MOF for comparison. The subsequent subpanels (ii)–(viii) in both (a) and (b) correspond to the individual samples studied: (ii) ZnFe MOF, (iii) ZnFe 12, (iv) ZnFe 24, (v) ZnFe 1:1, (vi) ZnFe 2:1, (vii) ZnFe 100, and (viii) ZnFe 140. These spectra allow a clear comparison of the Zn and Fe chemical states across the different compositions and synthesis conditions.*

Elemental Mapping

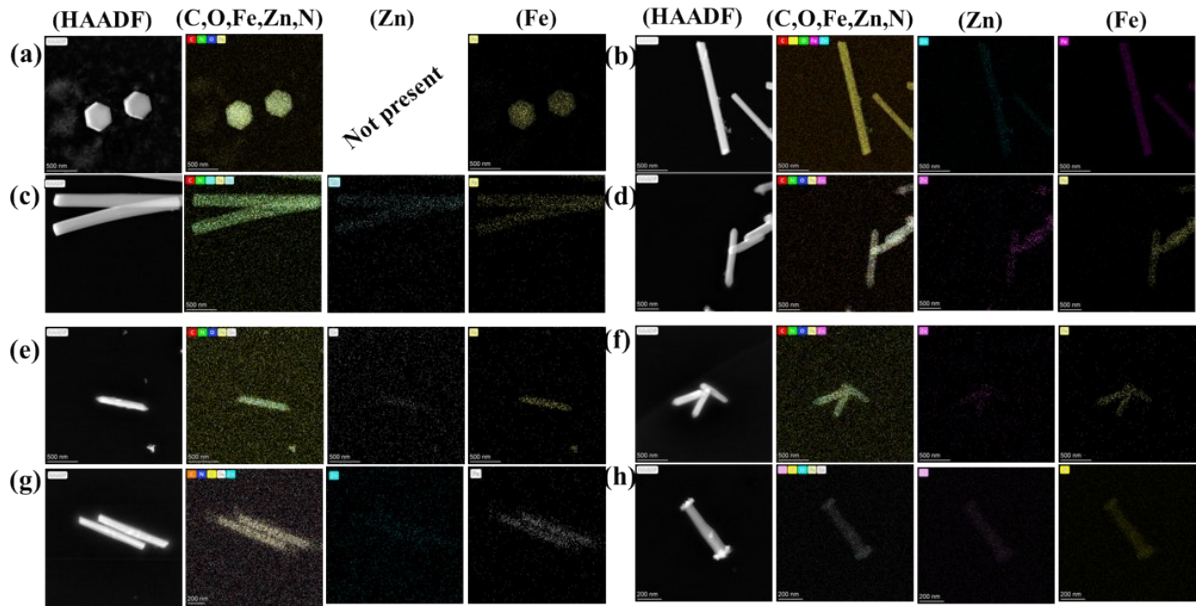

Figure S6*: Elemental composition analysis of MOFs using TEM-EDAX, with elemental identities indicated at the top of each spectrum: (a) Fe-MOF, (b) ZnFe-12, (c) ZnFe-MOF, (d) ZnFe-24, (e) ZnFe-1:1, (f) ZnFe-100, (g) ZnFe-2:1, and (h) ZnFe-140.*

BET Surface Area

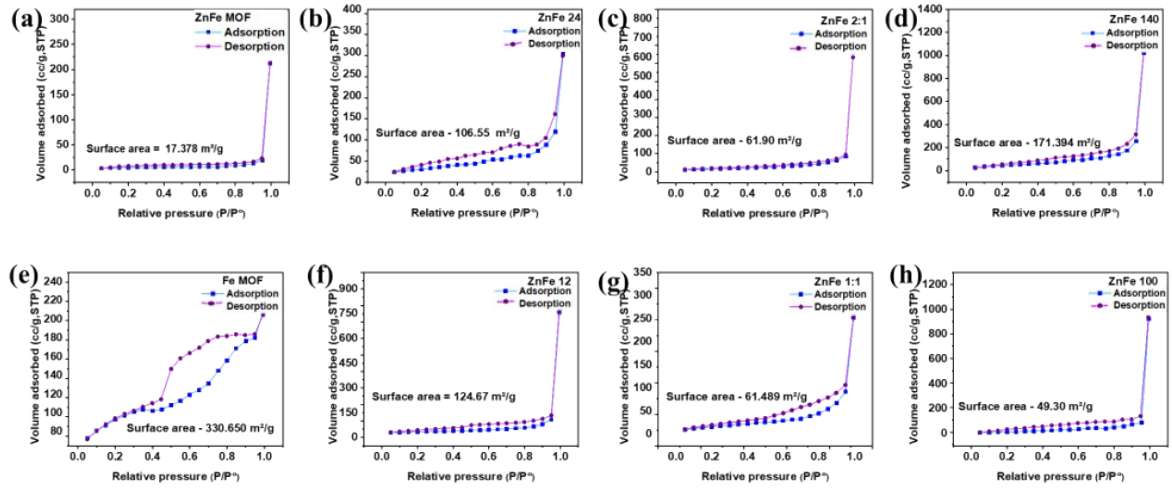

Figure S7*: BET surface area analysis of (a) ZnFe-MOF, (b) ZnFe-24, (c) ZnFe-2:1, (d) ZnFe-140, (e) Fe-MOF, (f) ZnFe-12, (g) ZnFe-1:1, and (h) ZnFe-100, illustrating the textural properties and porosity variations among the synthesized MOFs.*

BJH Pore Size

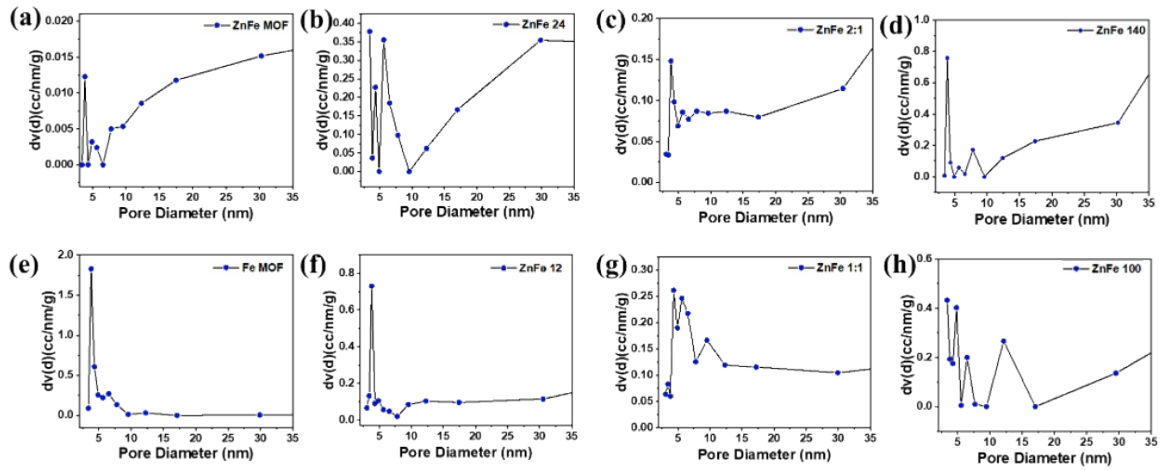

Figure S8*: BJH pore size distribution of (a) ZnFe-MOF, (b) ZnFe-24, (c) ZnFe-2:1, (d) ZnFe-140, (e) Fe-MOF, (f) ZnFe-12, (g) ZnFe-1:1, and (h) ZnFe-100, highlighting the mesoporous characteristics and structural variations of the synthesized MOFs.*

TGA (Thermogravimetric Analysis)

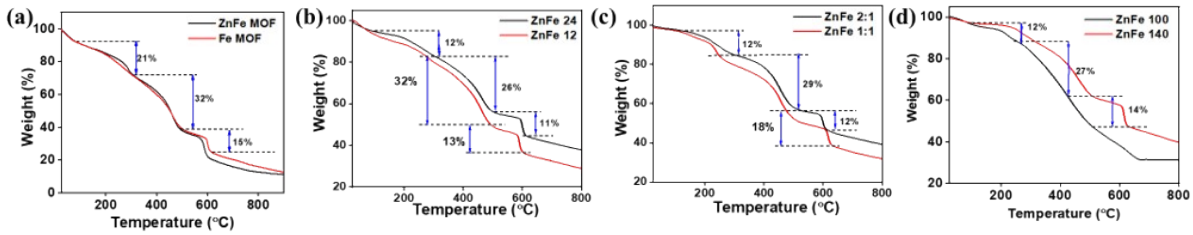

Figure S9*- Thermogravimetric analysis (TGA) of MOF samples: (a) Comparison between ZnFe-MOF and Fe-MOF; (b) Effect of reaction time; (c) Influence of solvent; (d) Impact of synthesis temperature on thermal stability.*

RAMAN

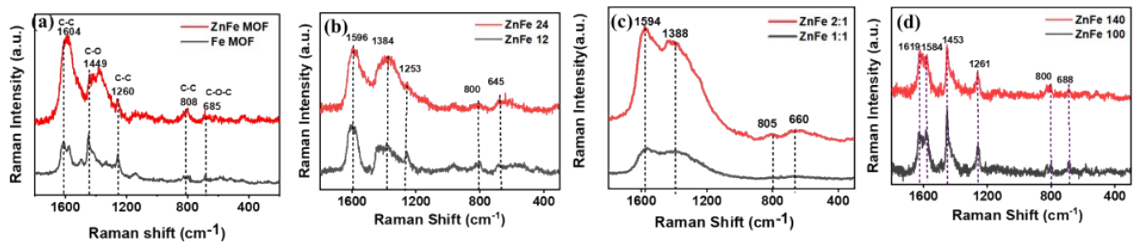

Figure S10- *Raman spectra of ZnFe-MOF samples synthesized under varying conditions: (a) Effect of reaction time, (b) Influence of solvent, (c) Impact of synthesis temperature on molecular structure.*

Breathing Behaviour

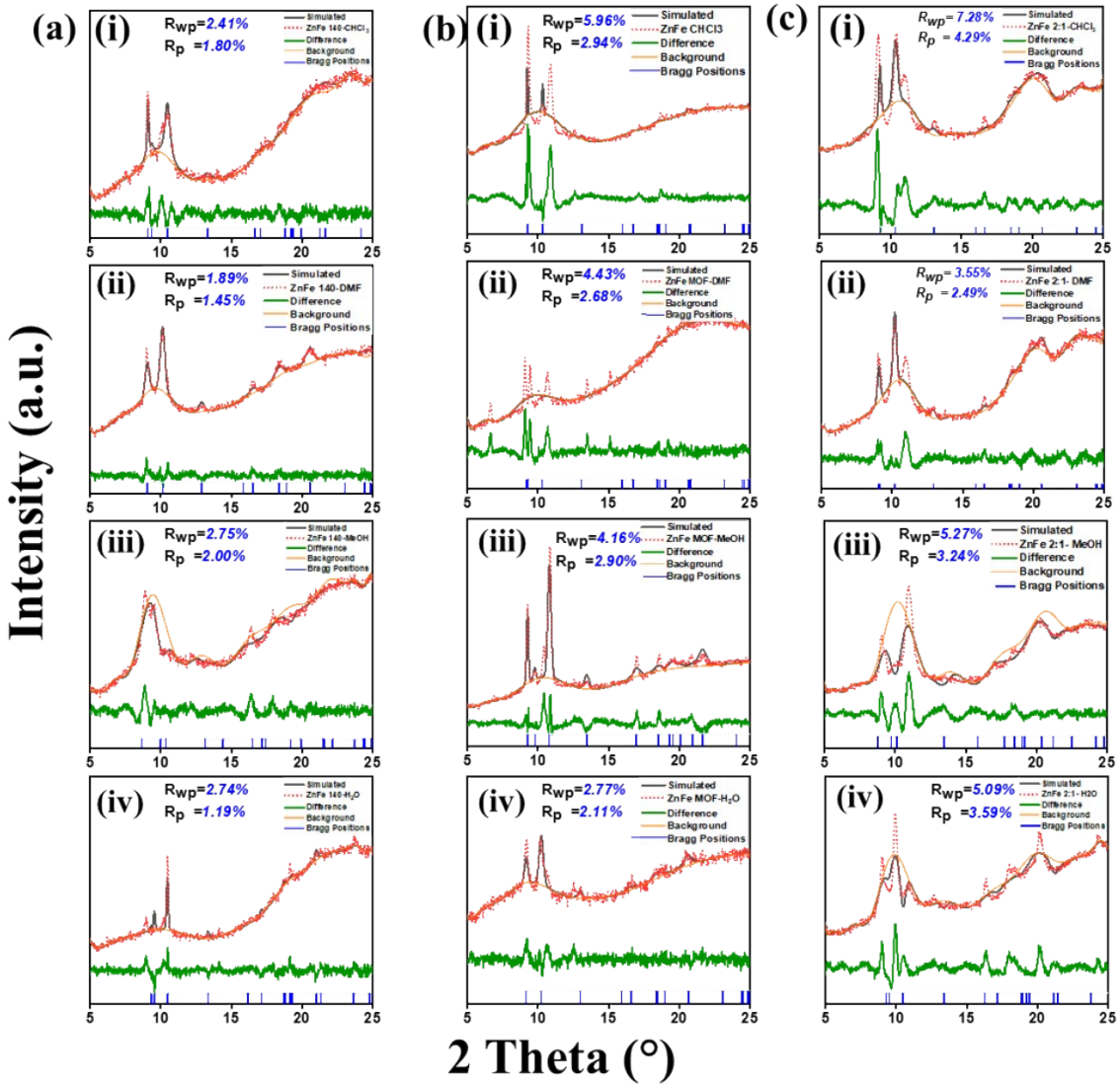

***Figure* S11-** *Rietveld Refined patterns of (a) ZnFe 140 (b) ZnFe MOF, (c) ZnFe 2:1, Where (i)$CHCl_3$, (ii) DMF, (iii) MeOH and (iv) H_2O represents different solvents in which respective samples were soaked. The grey lines are simulated graph NH_2-MIL-88B , orange lines are obtained PXRD pattern of different MOFs , green lines are difference between simulated and obtained pattern , yellow lines are background line and blue drop lines are Bragg's positions.*

Fluorescence

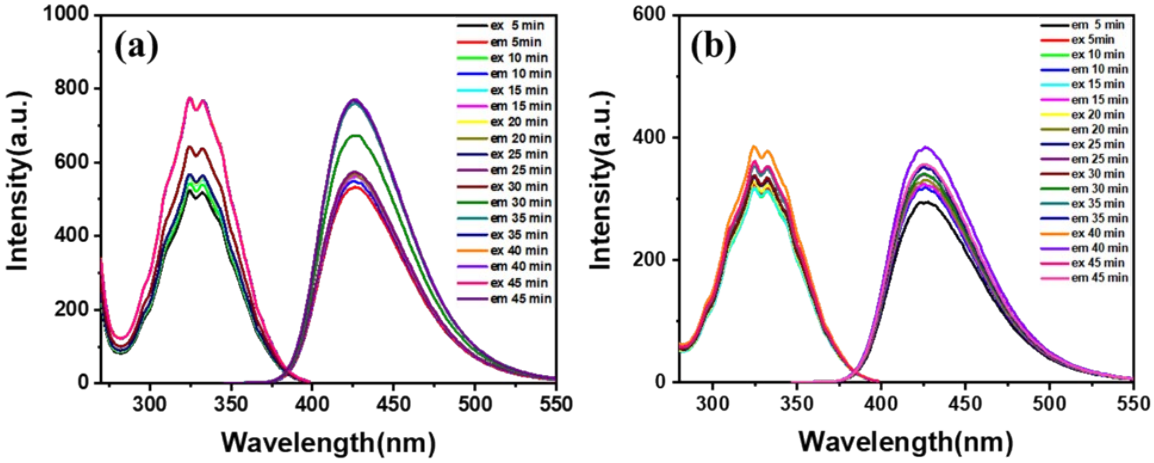

Figure S12*: Time-dependent fluorescence spectra of (a) ZnFe-MOF and (b) Fe-MOF, illustrating the evolution of fluorescence behaviour over time.*

Dopamine Sensing

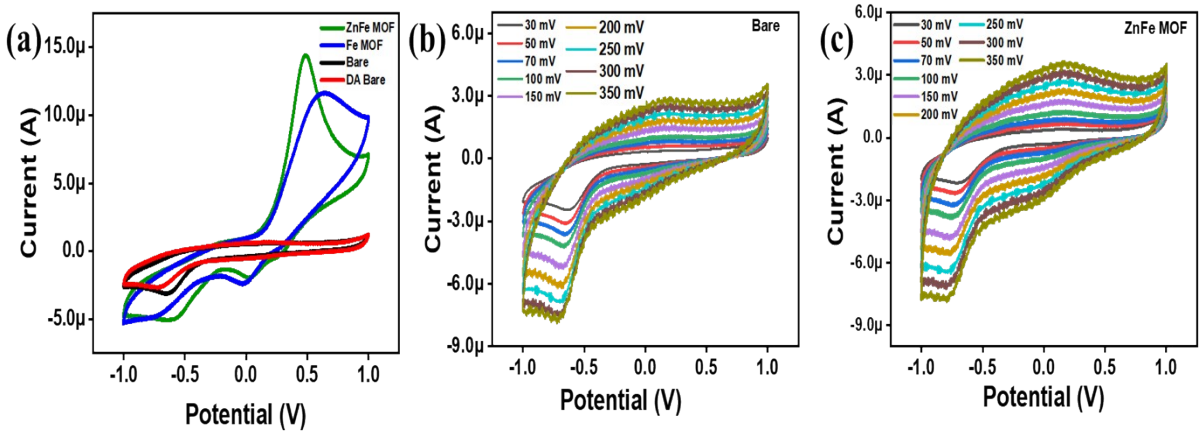

Figure S13: *(a) Comparison of ZnFe MOF with Fe MOF under same conditions for Dopamine sensing (b) Bare GCE at varying applied potential and (c) ZnFe MOF modified GCE with varying applied potential.*

Table S1: *Summary of crystallite size, lattice constants, cell volume, space group and crystallographic Rietveld refinement parameters for the MOF samples.*

Sample: Hexagonal structure (a=b ≠c)	**Crystallite Size (nm)**	**a(Å)**	**b(Å)**	**c(Å)**	**Cell Volume ($Å^3$)**	**Space Group**	**R_P (profile R-factor) %**	**R_{WP} (weighted profile R-factor) %**	**R_{WP} (w/o) back (%)**
Fe MOF	19.5	10.54	10.54	19.012	1828.86	P$\bar{6}$2c	1.85	2.86	33.94
ZnFe MOF	22.8	11.27	11.27	19.212	2440	P$\bar{6}$2c	3.07	4.56	24.87
ZnFe 12	26.2	11.212	11.212	19.268	2422	P$\bar{6}$2c	3.00	4.22	32.23
ZnFe 24	28.6	10.96	10.96	19.18	2303	P$\bar{6}$2c	3.24	4.89	25.67
ZnFe 1:1	35.7	11.42	11.42	19.50	2543.38	P$\bar{6}$2c	7.64	11.39	87.64
ZnFe 2:1	38.3	10.027	10.027	19.417	1949.47	P$\bar{6}$2c	7.43	12.25	85.25
ZnFe 100	31.6	10.72	10.72	19.299	2234.46	P$\bar{6}$2c	3.22	4.27	36.72
ZnFe 140	19.7	10.80	10.80	19.120	2230.22	P$\bar{6}$2c	2.41	3.29	34.80

Table S2: *XPS atomic weight percentage of Zinc, Iron, Oxygen, Nitrogen and Carbon in all MOFs.*

XPS	**Sample**	**Zn 2p**	**Fe 2p**	**O1s**	**N1s**	**C1s**
1	**ZnFe MOF**	2.31	2.71	25.16	7.43	62.39
2	**ZnFe 24**	1.44	2.05	24.59	5.92	61.52
3	**ZnFe 12**	2.95	4.89	24.87	7.11	64.02
4	**ZnFe 1:1**	2.9	2.1	26.45	7.72	60.82
5	**ZnFe 2:1**	0.72	5.41	28.69	6.41	58.77
6	**ZnFe 100**	1.41	2.02	33.42	3.86	58.29
7	**ZnFe 140**	2.65	4.09	27.49	6.01	59.76
8	**Fe MOF**	Not present	3.57	25.03	3.93	58.68

***Table S3**: Breathing Behaviour -Variation in width in various solvents of ZnFe 140, ZnFe MOF and ZnFe 2:1.*

Solvent	**ZnFe 140**	**ZnFe MOF**	**ZnFe 2:1**
	Particle width (nm)		
Water	87	191	92
Methanol	96	215	108
DMF	111	228	121
Chloroform	130	240	160
Original	115	258	141

***Table S4**: Breathing Behaviour -Variation via Rietveld refinement in various MOFs ZnFe 140, ZnFe MOF and ZnFe 2:1.*

	ZnFe 140			**ZnFe MOF**			**ZnFe 2:1**		
Solvent	**R_P(%)**	**R_{WP}(%)**	**R_{WP} (w/o) back (%)**	**R_P(%)**	**R_{WP}(%)**	**R_{WP} (w/o) back (%)**	**R_P(%)**	**R_{WP}(%)**	**R_{WP} (w/o) back (%)**
$CHCl_3$	1.80	2.41	49.20	2.94	5.96	94.51	4.29	7.28	62.72
DMF	1.45	1.89	30.61	2.68	4.43	99.93	2.49	3.55	56.31
MeOH	2.00	2.75	47.34	2.90	4.16	38.7	3.24	5.27	37.90
H_2O	1.91	2.74	65.80	2.11	2.77	62.99	3.59	5.09	68.64

****Rp(Profile Residual) , Rwp(Weighted Profile Residual) and Rwp (without background).***

Table S5*: Comparison table of recently reported Dopamine sensors with their linear range and limit of detection.*

Material choice	**Linear range**	**LOD Detection limit (µM)**	**Ref**
ZnFe MOF	10 µM- 1000 µM	0.043 µM	This work
Ni/Ag/Zn trimetallic oxide	1−25 µM	0.3 µM	1
ZnO/$Ti_3C_2T_x$/Nafion/Au	0.1 – 1200 µM	0.076 µM	2
ZnO/MWNTs/GCE	3–200 µM	3 µM	3
Fe_2Ni MIL-88B/GCE	1.2 µM–1.8 mM	0.40 µM	4
AgPd@Zr-MOF/GCE	2–42 µM	0.1 µM	5
Au@Cu-MOF	10 µM to 1000 µM	3.40 µM	6
MOF-5@MWCNT	0.1–60 µM	0.0075 µM	7
Fe_3O_4@ZIF-8@AuNPs–COOH	0.05–120 µM	26 nM	8
Co/Zn-TCPP	5 nM–177.8 µM	1.67 nM	9
ZrNi-Fc MOF	0.1–70 µM	0.07 µM	10

References

1. Zhang, W., Sharma, G., Kumar, A., Shekh, M. I. & Stadler, F. J. Fabrication and characterization of Ni/Ag/Zn trimetal oxide nanocomposites and its application in dopamine sensing. *Mater. Today Commun.* **29**, (2021).
2. Cao, M. *et al.* Preparation of ZnO/Ti3C2Tx/Nafion/Au electrode. *Microchemical Journal* **175**, (2022).
3. Aravind, S. S. J. & Ramaprabhu, S. Dopamine biosensor with metal oxide nanoparticles decorated multi-walled carbon nanotubes. *Nanoscience Methods* **1**, 102–114 (2012).
4. Duan, C. & Zheng, J. Bimetallic MOF-Based Enzyme-Free Sensor for Highly Sensitive and Selective Detection of Dopamine. *J. Electrochem. Soc.* **166**, B942–B947 (2019).
5. Hira, S. A., Nagappan, S., Annas, D., Kumar, Y. A. & Park, K. H. NO2-functionalized metal–organic framework incorporating bimetallic alloy nanoparticles as a sensor for

efficient electrochemical detection of dopamine. *Electrochem. commun.* **125**, 107012 (2021).

6. Zhou, F. *et al.* Simultaneous Electrochemical Detection of Dopamine and Uric Acid via Au@Cu-Metal Organic Framework. *Chempluschem* **89**, (2024).
7. Gu, J., Lang, S., Jin, Z. & Wei, T. A Dual-Functional and Efficient MOF-5@MWCNTs Electrochemical Sensing Device for the Measurement of Trace-Level Acetaminophenol and Dopamine. *Molecules* **29**, (2024).
8. Guo, J., Ma, Y., Han, T., Yang, J. & Miao, P. Magnetic MOF composites for the electrocatalysis and biosensing of dopamine released from living cells. *J. Mater. Chem. B* **12**, 8181–8188 (2024).
9. Ma, J., Bai, W., Liu, X. & Zheng, J. Electrochemical dopamine sensor based on bi-metallic Co/Zn porphyrin metal–organic framework. *Microchimica Acta* **189**, (2022).
10. He, X. *et al.* Ferrocene-Based Zr/Ni Bimetal–Organic Frameworks for Ratiometric Aptamer Sensors Enabling Efficient Dopamine Detection. *Anal. Chem.* https://doi.org/10.1021/acs.analchem.5c06788 (2026) doi:10.1021/acs.analchem.5c06788.